The dependence of F-region electron heating on HF radio pump power: Measurements at EISCAT Tromsø

A. Senior,[1] M. T. Rietveld,[2] T. K. Yeoman,[3] and M. J. Kosch[1,4]

Received 14 October 2011; revised 25 January 2012; accepted 22 February 2012; published 10 April 2012.

[1] Measurements of ionospheric electron temperature enhanced by the action of a powerful high-frequency radio wave on the F-region at the EISCAT facility near Tromsø, Norway are analyzed to obtain the electron heat source due to the radio wave as a function of transmitter power. The absorption of the wave in the D-region is accounted for and is found to have a significant influence on the F-region heating, especially due to variations in the D-region electron density during the experiment. It is found that the efficiency of F-region heating expressed in terms of the electron heating rate as a function of radio wave power flux is higher at higher transmitter powers. This behavior seems to be consistent with the development of geomagnetic field-aligned plasma density irregularities which are associated with the conversion of the radio wave to electrostatic upper-hybrid waves. At the highest power fluxes, the efficiency appears to be close to 100%.

Citation: Senior, A., M. T. Rietveld, T. K. Yeoman, and M. J. Kosch (2012), The dependence of F-region electron heating on HF radio pump power: Measurements at EISCAT Tromsø, *J. Geophys. Res.*, *117*, A04309, doi:10.1029/2011JA017267.

1. Introduction

[2] Geomagnetic field-aligned plasma density irregularities (FAI) in the F-region of the ionosphere generated by the action of a powerful high-frequency (HF) radio wave were first detected using the facility at Platteville, Colorado [*Thome and Blood*, 1974]. The phenomenon was subsequently detected at other high-power HF facilities, including at Tromsø, Norway where it was associated with large enhancements of the electron temperature by incoherent scatter radar measurements [*Jones et al.*, 1986].

[3] The generation of FAI is explained theoretically in terms of a thermal parametric instability (TPI), reviewed by *Robinson* [1989]. An O-mode radio wave (the "pump") is converted to electrostatic upper-hybrid (UH) waves in the vicinity of the UH resonance level, where the local plasma upper-hybrid frequency equals the radio wave frequency, by scattering on plasma density irregularities. Plasma heating by the electric field of the UH waves reinforces the irregularities, leading to an instability.

[4] *Robinson et al.* [1996] found that the amplitude of FAI as measured by anomalous absorption and the electron temperature enhancement both minimized when the pump frequency was close to the third or fourth electron gyroharmonic frequencies where excitation of UH waves is expected to be suppressed. This minimization of FAI, electron temperature and additionally electron acceleration as indicated by optical emissions has been confirmed several times [*Honary et al.*, 1999; *Kosch et al.*, 2002; *Gustavsson et al.*, 2006]. This suggests that at high latitudes, the excitation of UH waves and FAI are the major source of electron heating, though other mechanisms are not excluded. The behavior around the second gyroharmonic is an exception: *Kosch et al.* [2009] found that electron heating maximized around the second gyroharmonic.

[5] The relationship between the electron heat source and the available pump power for overdense F-region heating has been examined before in a number of cases [*Mantas et al.*, 1981; *Robinson*, 1989; *Stocker et al.*, 1992]. Heating in underdense conditions at Tromsø has been modeled by *Gustavsson et al.* [2010] and good agreement between observations and theory was found on the basis that the heating is due to the electric field of the electromagnetic pump wave alone. However, *Gustavsson et al.* [2010] did not explicitly quantify the efficiency of this mechanism, which is of interest here. In the present work, experimental data in which the pump power was systematically varied are analyzed to determine the electron heating rate as a function of available radio wave power flux and hence the efficiency of the heating mechanism. It is found that the mechanism becomes more efficient at higher power fluxes, which is consistent with the development of FAI and conversion of the pump wave to UH waves. It is also found that the absorption of the pump wave in the D-region is highly variable and plays a significant role in determining the power flux reaching the F-region.

2. Experiment

[6] The experiment analyzed here was performed on 14 November 2006 from 10–12 UT. The F-region plasma was pumped using the European Incoherent Scatter (EISCAT) HF

[1]Department of Physics, University of Lancaster, Lancaster, UK.
[2]EISCAT Scientific Association, Ramfjordbotn, Norway.
[3]Department of Physics and Astronomy, University of Leicester, Leicester, UK.
[4]Also at School of Physics, University of KwaZulu-Natal, Durban, South Africa.

0148-0227/12/2011JA017267

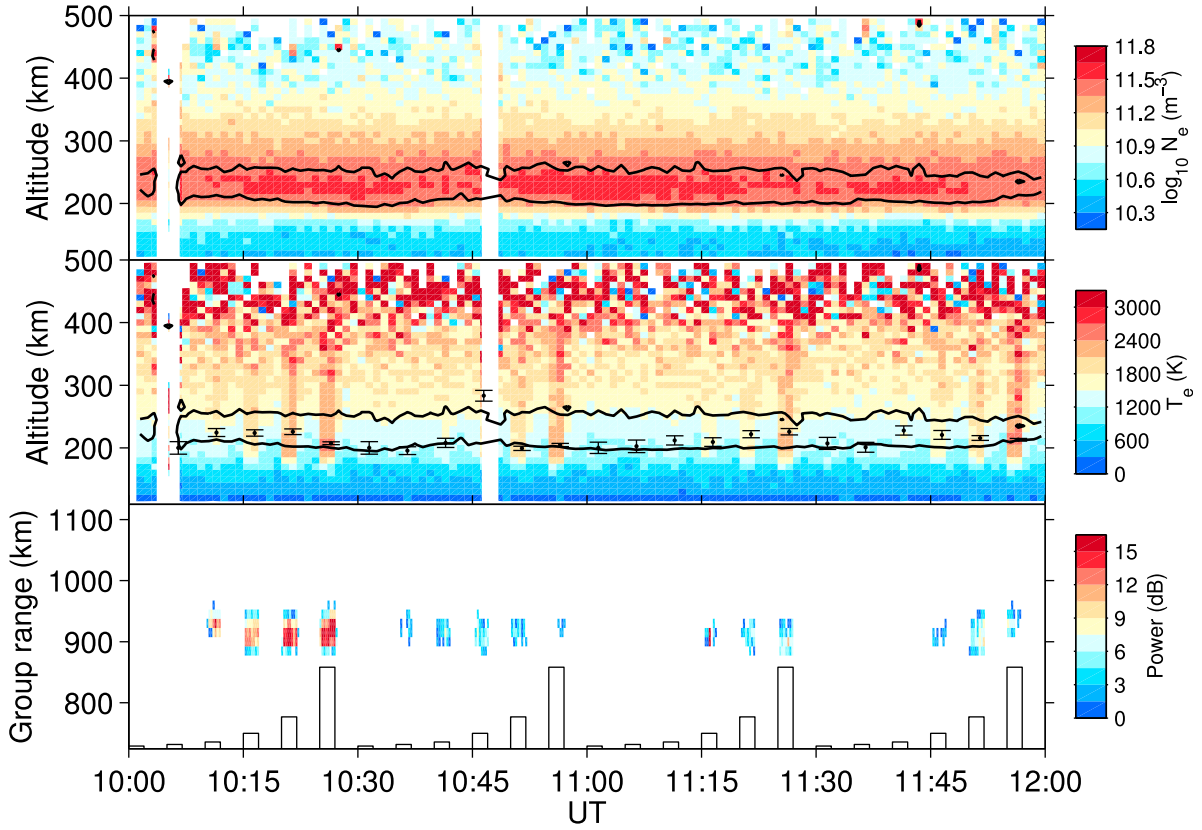

Figure 1. (top) The electron density profiles measured by the UHF radar. The altitude where the plasma upper-hybrid frequency matches the pump frequency is marked by the black contour. (middle) The electron temperature profiles measured by the UHF radar. The black points with error bars indicate the estimated altitude of the peak of the electron heat source due to the pump wave, determined from the analysis of section 3.1. The black line is again the UH resonance contour. (bottom) The backscatter power received by the CUTLASS Hankasalmi radar. The black rectangles denote the pump on-off cycle, the height of each rectangle indicating the relative pump ERP.

facility, near Tromsø, Norway (69.58°N, 19.21°E) operated on 4.9128 MHz using O-mode polarization with the beam directed 12° south of the zenith, approximately geomagnetic field-aligned in the F-region. The full width of the beam at half-maximum power was 12°. The frequency chosen is far from a harmonic of the electron gyrofrequency. The pump wave was cycled 2 minutes on, 3 min off starting at 10:00 UT. On successive cycles, the pump power was increased in the sequence 3.2, 5.1, 8.2, 19, 39 and 100% of full power, which in this case was 202 MW effective isotropic radiated power (ERP), assuming a perfectly reflecting ground beneath the antennae. This sequence of power steps was repeated four times during the two-hour interval. The facility has been described by *Rietveld et al.* [1993].

[7] The EISCAT UHF radar [*Rishbeth and van Eyken*, 1993], almost co-located with the HF facility, observed the ionosphere with the beam directed parallel to the that of the HF facility. The radar ran a variant of the standard *tau2pl* program which differed only in the handling of the plasma line measurements which are not used in this study. The ion-line measurements cover 45–700 km range, though toward the lower altitudes, the data do not allow the spectrum to be fully resolved. The data were analyzed at 60 s temporal resolution with plasma parameters being fitted with 10 km altitude resolution from 110 km to 500 km. Additionally, measurements of the shortest non-zero lags were used to determine the electron density down to 60 km. The electron densities were calibrated against the EISCAT Dynasonde [*Rietveld et al.*, 2008] and were correct to ±5%.

[8] The Co-operative UK Twin-Located Auroral Sounding System (CUTLASS) HF radar at Hankasalmi, Finland (62.32°N, 26.61°E), part of the SuperDARN network [*Greenwald et al.*, 1995; *Chisham et al.*, 2007], observed the F-region over EISCAT on five frequency bands sequentially on a single beam. The range resolution was 15 km and the integration time on each frequency was 3 s. Each frequency band was revisited every 15–16 s. The strongest backscatter from pump-induced plasma density irregularities was received on the 19 MHz band and only data from this band are considered in this study. The radar is described in more detail by *Lester et al.* [2004].

[9] Figure 1 summarizes the EISCAT and CUTLASS radar observations during the experiment. The top panel shows the electron density profile as a function of time. The upper-hybrid resonance contour, where the pump frequency matches the local plasma upper-hybrid frequency is marked. The lower part of this contour, below the reflection height of the pump wave is where the pump wave is expected to be

converted to upper-hybrid waves [*Robinson*, 1989]. The blank vertical stripes denote areas where the radar transmitter was down and measurements were not available. The middle panel of Figure 1 shows the electron temperature profile as a function of time. The heating and cooling of the electrons due to the pumping is clearly seen during the last (highest) three power steps of each sequence. Finally, the bottom panel shows the backscatter power received by the CUTLASS radar as a function of time and group (virtual) range from the radar. Once again, the pump on-off cycle is clearly seen by the appearance and disappearance of backscatter, though not all pump-on periods produced detectable backscatter.

3. Analysis

3.1. Retrieval of Heating Rates

[10] In equilibrium, the electron temperature T_e along a geomagnetic field-line in the F-region satisfies [*Schunk and Nagy*, 1978]

$$\sin^2 I \frac{\partial}{\partial z}\left[K_e(T_e,z)\frac{\partial T_e}{\partial z}\right] + Q_{\text{photo}}(z) + Q_{\text{RF}}(z) - L(T_e,z) = 0 \quad (1)$$

where z is altitude, $K_e(T_e, z)$ is the electron thermal conductivity and $L(T_e, z)$ is the electron cooling rate. $Q_{\text{photo}}(z)$ represents heating due to photoionization and $Q_{\text{RF}}(z)$ is an additional heat source due to electron heating by the pump wave and plasma waves stimulated by it. I is the inclination angle of the geomagnetic field; $I \approx 78^\circ$ in this case hence $\sin^2 I = 0.96$ and this factor is neglected.

[11] In this study, the aim is to determine the source $Q_{\text{RF}}(z)$ as a function of the pump power. When the pump is off and the electrons have cooled back to their undisturbed temperature, $Q_{\text{RF}}(z)$ is zero and (1) can be used to find the source $Q_{\text{photo}}(z)$. Assuming that this remained the same during the previous pump-on period, (1) can again be used to find $Q_{\text{RF}}(z)$. Although (1) could be solved directly for the sources, doing so is prone to error due to magnification of the measurement uncertainties in the derivative term in particular. Instead, (1) was solved by fitting a model source term, solving (1) for $T_e(z)$ and minimizing the least squares error between the solution and the observed electron temperature profile. The boundary conditions used in solving (1) were that at the lower boundary (110 km) $T_e = T_i$ where T_i is the ion temperature and that at the upper boundary (500 km), $\partial T_e/\partial z = 0$.

[12] For $Q_{\text{photo}}(z)$, the source was assumed to have a Gaussian profile in altitude with independent upper and lower half-widths

$$Q_{\text{photo}}(z) = \frac{2J_{\text{photo}}}{\sqrt{\pi}(H_L + H_U)} \exp\left(-\zeta^2\right) \quad (2)$$

$$\zeta = \begin{cases} (z - z_0)/H_L & (z < z_0) \\ (z - z_0)/H_U & (z \geq z_0) \end{cases} \quad (3)$$

[13] The fitted parameters are then the height-integrated heating rate J_{photo}, the altitude of the maximum z_0 and the two half-widths, H_L, H_U. For $Q_{\text{RF}}(z)$ a simple Gaussian profile in altitude was assumed, the fitted parameters being J_{RF}, z_0 and the half-width $H = H_L = H_U$.

[14] The source $Q_{\text{photo}}(z)$ was retrieved by fitting the model to the last 60 s of each pump on-off cycle and the source $Q_{\text{RF}}(z)$ by fitting to the last 60 s of each pump-on period, keeping $Q_{\text{photo}}(z)$ identical to that found during pump-off. It might be thought that since the pump has only been on for 60–120 s during this interval that the use of the equilibrium model (1) is questionable. However, in this case at least, it was found that even at the highest altitudes where reliable measurements could be obtained, there was no significant change in temperature over the 60–120 s period after pump-on when the data were analyzed with 20 s resolution and so the assumption of equilibrium is expected to be a good approximation.

[15] Due to the gaps in the radar data, the 1st on-off cycle could not be analyzed because the last 60 s of the pump-off period was missing. Also, for the 2nd cycle, only the last 20 s of the pump-on period was available and for the 10th cycle, only the last 60–75 s of the pump-on period was available. Consequently, lower confidence should be attached to the analysis of these cycles.

[16] The contributions to the electron cooling term considered here are from six processes: vibrational excitation of N_2 [*Campbell et al.*, 2004], rotational excitation of N_2 [*Pavlov*, 1998a], vibrational excitation of O_2 [*Jones et al.*, 2003], rotational excitation of O_2 [*Pavlov*, 1998b], excitation of the $O(^1D)$ state [*Schunk and Nagy*, 1978] and elastic collisions with ions. Cooling due to the latter was calculated using the electron-ion collision frequency given by *Schunk and Nagy* [2000, equation (4.144)] in the cooling rate expression equation (37) of *Schunk and Nagy* [1978]. Cooling due to fine structure excitation of atomic oxygen, found to be significant by *Schunk and Nagy* [1978], was neglected in the light of the work of *Pavlov and Berrington* [1999].

[17] The electron thermal conductivity was given by an expression due to Banks, equation (5.146) of *Schunk and Nagy* [2000]. Banks' approximation requires that the electron mean free path be significantly less than the electron temperature scale height. In the present data set, the scale height was found to be at least ten times the mean free path at all altitudes. The Maxwellian-averaged momentum transfer collision cross-sections of *Schunk and Nagy* [1978] were used in this expression. For both the thermal conductivity and cooling rates, the densities of neutral species were taken from the MSISE-90 model [*Hedin*, 1991].

[18] As detailed in the Appendix, it was found that the ion temperatures from the standard analysis of the UHF radar had an anomalous peak at 185 km. The procedure described in the Appendix was used to correct this problem. For the electron temperature modeling, the ion temperature and composition profiles were taken from the analysis described in the Appendix and were thus assumed constant throughout the two-hour experiment. The electron density profile was taken as the median of that over each complete 5-minute pump on-off cycle. Note that no significant difference was observed between the electron density profiles during pump-on and pump-off.

[19] It was found that at the high altitudes in particular, the electron temperature data were very noisy, but that this noise was not always reflected in the estimated measurement error. This caused problems in fitting the model since too high a weight was assigned to unreliable data points. To guard against this problem, the electron temperature profiles were

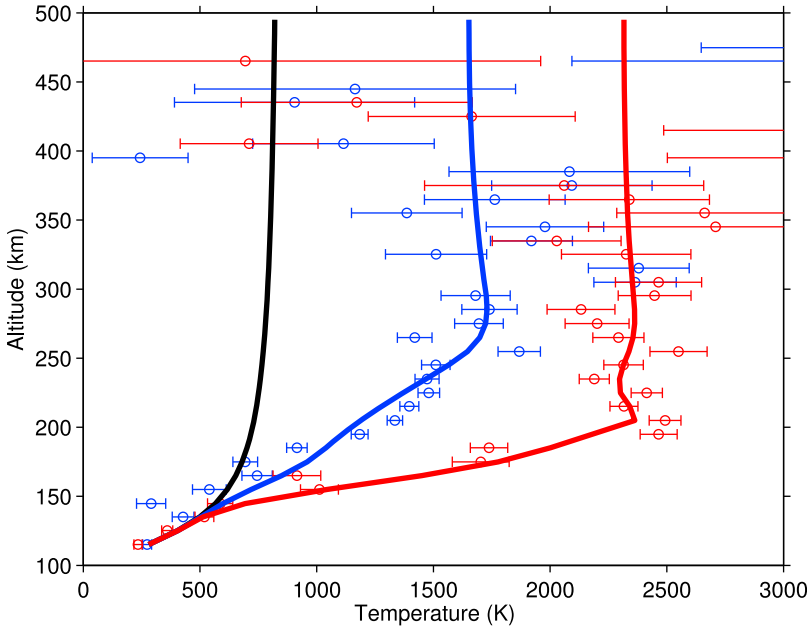

Figure 2. Example of fitting the model of equation (1) to the measured electron temperatures, for the pump cycle commencing at 10:25 UT. The ion temperature, determined by the procedure described in the Appendix, is shown in black. The blue circles with error bars are the measured electron temperatures during pump-off (10:29–10:30 UT). The red circles with error bars are the measured electron temperatures during pump-on (10:26–10:27 UT). The blue curve is the model fit to the pump-off data including only the photoionization heat source. The red curve is the model fit to the pump-on data including the pump-related heat source in addition to photoionization.

filtered by comparing the logarithm of the electron-ion temperature ratio at each altitude (the actual parameter fitted in the radar analysis) to the 5-point running median of this variable along the profile. Altitudes where the difference exceeded 5 times the error of the logarithm of the temperature ratio were excluded from the fit. This process eliminates both points with extreme values of electron temperature and those with unrealistically small error estimates.

[20] To stabilize and speed up the fitting process, prior estimates of the fitted parameters were used. For $Q_{\mathrm{photo}}(z)$, the prior values were $J_{\mathrm{photo}} = 10\ \mu\mathrm{W\ m^{-2}}$, $z_0 = 300$ km, $H_L = H_U = 50$ km with standard errors of 10 μW m^{-2}, 50 km and 20 km respectively. For $Q_{\mathrm{RF}}(z)$, the values were $J_{\mathrm{RF}} = 0\ \mu\mathrm{W\ m^{-2}}$, $z_0 = 200$ km, $H = 5$ km with standard errors of 50 μW m^{-2}, 10 km and 2 km respectively. Figure 2 shows the results of fitting the model to the measurements for the pump cycle commencing at 10:25 UT (100% pump power).

[21] The fitted height-integrated heating rates due to photoionization and HF pumping are summarized in Figure 3 and the fitted peak altitudes z_0 of the heat source Q_{RF} are shown in Figure 1 (middle). The heating due to photoionization shows a broad peak in the early part of the interval, which is consistent with local noon occurring near 10:40 UT. The heating due to HF pumping clearly increases as the pump power is increased through each 30-minute cycle, but there is considerable variation from cycle to cycle with the third cycle showing only about 25% as much heating as the first cycle.

[22] The error estimates of the fitted heating rates are based on the estimated errors in the measured electron temperatures only. Additional random error arises from the use of measured electron densities in the model. The model fits were not always good, showing some tendency to bias in the residuals (see Figure 2). This indicates some systematic error in the model or in the analyzed radar data. For these reasons, the error estimates of the fitted heating rates should be considered underestimates.

3.2. D-region Absorption of the Pump Wave

[23] Figure 4 shows the median D- and E region electron density profile over each of the four 30-minute intervals corresponding to the four cycles of pump power steps. It is clear that small but significant changes occur in the D-region between these intervals. For example, the density at 80 km during 10:30–11:00 UT and 11:00–11:30 UT is approximately double that during 10:00–10:30 UT. The high electron-neutral collision frequency in the D-region leads to strong absorption of the HF pump wave and the absorption is approximately proportional to electron density. Since the collision frequency depends on electron temperature and this is influenced by ohmic heating from the pump electric field, it is necessary to model the D-region absorption of the pump wave as a function of its power.

[24] The model described by *Senior et al.* [2010], which self-consistently calculates the absorption of the high-power radio wave due to ohmic heating of the electrons, was used to find the height dependence of the pump wave power flux as a function of pump ERP and electron density for each 30-minute pump power cycle. Steady state was assumed in

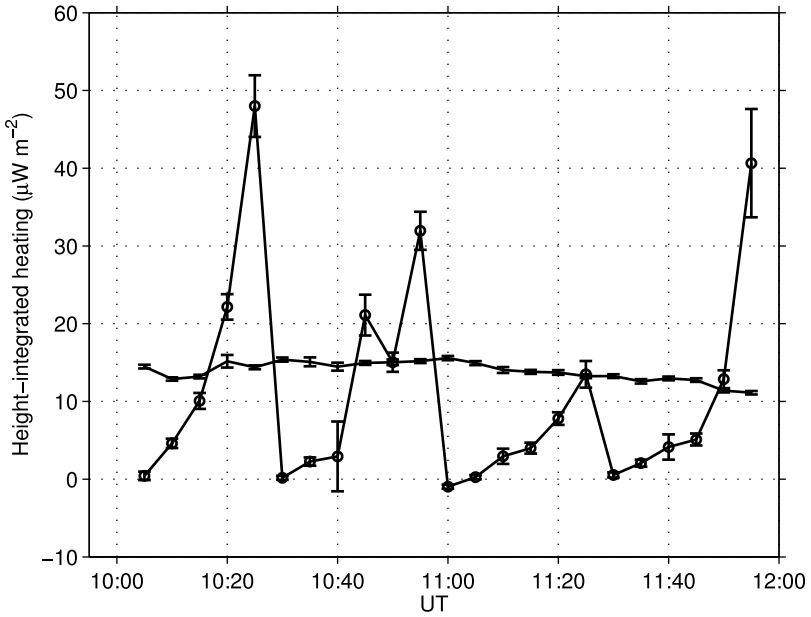

Figure 3. The fitted height-integrated heat sources for photoionization (line with error bars) and for pump-induced heating (line with error bars and circular markers).

the calculations since the heating and cooling times of the electrons in the D-region are of the order of 1 ms or less. Figure 5 shows the results for the cases of minimum and maximum pump power. Most of the absorption takes place between about 70 and 90 km altitude. It is clear that the absorption is higher in the cases with higher D-region electron densities and for higher pump ERP.

3.3. Relation of Heating Rate to Pump Power

[25] Using the results from the D-region model to account for the absorption and then assuming free-space propagation above 110 km altitude, the pump power fluxes, *S*, were calculated at an altitude of 202 km. This altitude was the UH resonance altitude obtained from the median electron density profile for the 2-hour experiment run, see Sec. 4.2. Taking

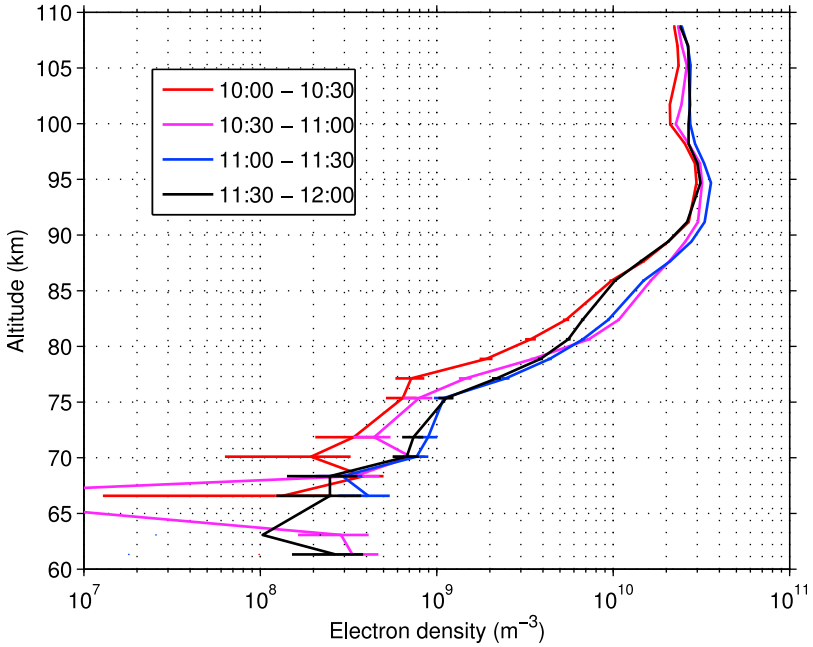

Figure 4. Median profiles of the electron density in the D- and E region over the four 30-minute intervals corresponding to the four cycles of pump power: 10:00–10:30 UT (red), 10:30–11:00 UT (magenta), 11:00–11:30 UT (blue) and 11:30–12:00 UT (black).

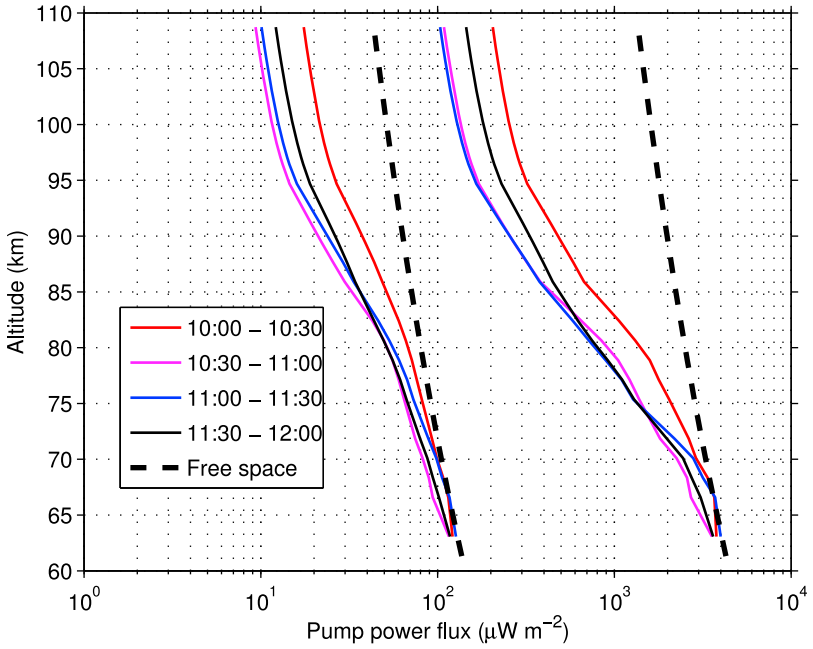

Figure 5. Profiles of the pump power flux in the D- and E regions for each 30-minute interval. The profiles are shown for the cases of minimum (3.2%) and maximum (100%) pump power. The dashed line shows the profile corresponding to no absorption.

into account the 12° zenith angle of the pump beam, this corresponds to a range of 207 km from the transmitter. The pump power fluxes were then compared with the height-integrated heating rates (J_{RF}) retrieved from the observations. The result is presented in Figure 6.

[26] As might be expected, the height-integrated heating rate increases with pump power flux. The local maximum around a power flux of 10 μW m^{-2} is probably just a consequence of random error and not a real feature. The two data points in Figure 6 marked with open squares are the 2nd (red) and 10th (magenta) on-off cycles which may be unreliable due to incomplete data as noted in Sec. 3.1.

[27] The efficiency, η, of the heating process can be defined as the ratio of the height-integrated heating rate to

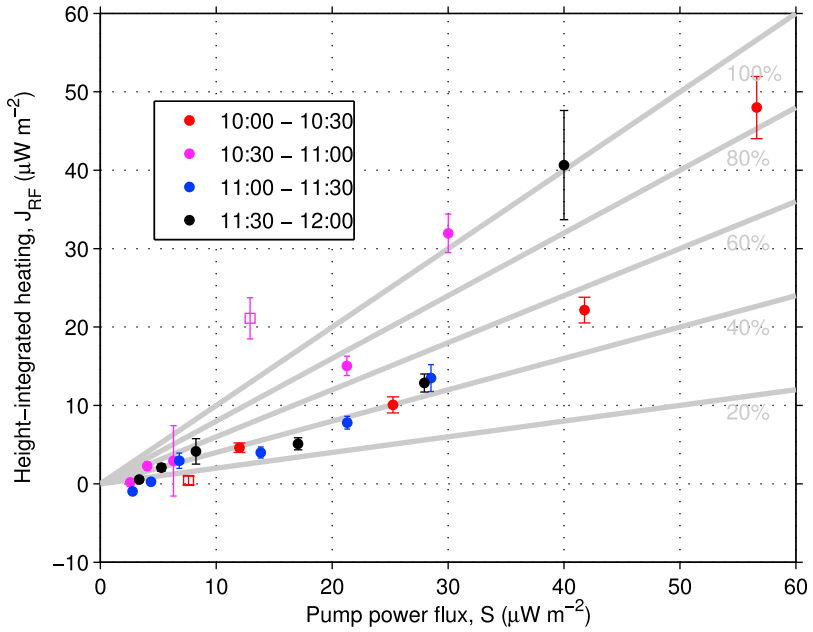

Figure 6. Height-integrated heating rate due to HF pumping versus the estimated pump power flux at 202 km altitude. The five gray lines of increasing slope indicate heating efficiencies $\eta = J_{RF}/S$ of 20, 40, 60, 80 and 100% respectively. The points marked with open squares may be unreliable due to incomplete radar data coverage.

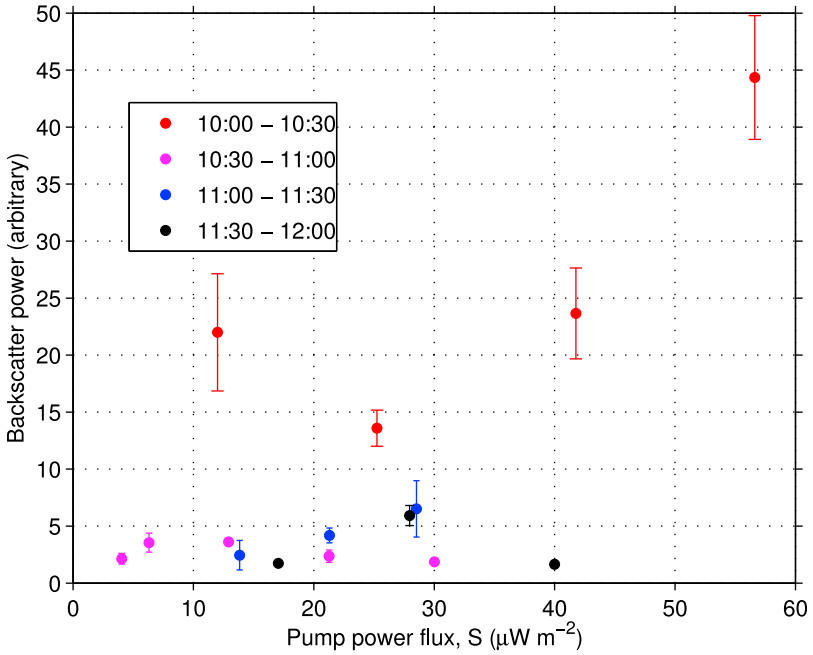

Figure 7. CUTLASS backscatter power (in arbitrary linear units) versus the estimated pump power-flux at 200 km altitude.

the pump power flux, $\eta = J_{RF}/S$. The gray sloping lines in Figure 6 indicate efficiencies of 20, 40, 60, 80 and 100%. It can be seen that the efficiency generally increases with the pump power flux, reaching 100% in some cases.

3.4. Relation of CUTLASS Backscatter to Pump Power

[28] The mean backscatter power measured by the CUTLASS radar over the last 60 s of each pump-on period was found. In Figure 7, the peak of this mean power over the range extent of the pump-induced backscatter patch is plotted against the same pump power flux used in Figure 6 for each pump on-off cycle. For low values of pump power flux (<25 μW m^{-2}), the backscatter power predominantly remains low, the exception being the case with the lowest power flux from the 10:00–10:30 UT power stepping sequence (red). At higher power fluxes, there is some evidence of a tendency for the backscatter power to increase with power flux, an exception here being the case with the highest power flux from the 11:30–12:00 UT power stepping sequence (black) which is unusually low.

4. Discussion

4.1. The Heating Mechanism and Its Efficiency

[29] The UH wave electric field resulting from conversion of the pump electric field on the small plasma density perturbation in FAI is proportional to the amplitude of the density perturbation in the irregularities

$$E_{\mathrm{UH}} = \frac{E_{\mathrm{EM}}}{\epsilon}\frac{\Delta N}{N} \tag{4}$$

where E_{EM} is the pump electric field, ϵ is the dielectric constant, N is the ambient plasma density and ΔN the density perturbation [*Dysthe et al.*, 1983]. As $|\epsilon| \approx 0$ at the UH resonance level, $E_{\mathrm{UH}} > E_{\mathrm{EM}}$ even for small density perturbations.

[30] Both theoretical considerations [*Robinson*, 1989] and experimental evidence [*Wright et al.*, 2006] show that for low pump power fluxes, the intensity of the excited FAI rapidly increases with pump power but then begins to approach a saturation level. Therefore, not only does the total electric field increase due to the increasing pump power, but also because of the increasing conversion of the electromagnetic pump wave to electrostatic UH waves. As the ohmic heating by the electric field is $\sigma|E|^2$ where σ is the conductivity, it is clear that the electron heating should be higher for higher FAI density depletions. In other words, the heating mechanism becomes more efficient at converting pump energy to heat as FAI are progressively developed.

[31] Figure 6 shows that the heating efficiency does increase with increasing heater power. The CUTLASS backscatter power is proportional to $(\Delta N/N)^2$ for the component of the irregularity wave number spectrum which satisfies the Bragg scattering condition (an irregularity wavelength of ~8 m for the radar frequency of 19 MHz) [*Booker*, 1956]. Therefore, Figure 7 shows, particularly for the periods 10:00–10:30 and 11:00–11:30, that the intensity of FAI also increases with heater power in agreement with the theory. The behavior of the FAI intensity shown in Figure 7 is not entirely convincing, but there is ample evidence from previous studies of FAI intensity both by radar backscatter and the anomalous absorption of diagnostic HF waves that the general picture of an initial rapid increase followed by a saturation in FAI intensity as the heater power is increased is correct [*Jones et al.*, 1983; *Hedberg et al.*, 1986; *Wright et al.*, 2006]. In the present case, some of the variability in the CUTLASS backscatter power may be due to the presence of atmospheric gravity wave (AGW) activity in the ionosphere during the experiment. *Senior et al.* [2006]

found that AGW disturbances can have a marked effect on the strength and location of backscatter due to EISCAT HF heating detected by CUTLASS. Evidence for AGW activity was apparent in ground-scatter returns on lower radar frequencies (not shown here) and is also the likely cause of the quasiperiodic changes in electron density in Figure 1, most evident around the peak of the F-region and in the variation of the UH resonance altitude.

[32] The efficiency at high pump powers is seen in Figure 6 to reach 100%. If this is true then it implies that nearly all the upgoing pump energy is converted into heat and in particular that the reflected pump wave should be very weak or absent. *Jones et al.* [1983] analyzed measurements of the reflected pump power at 5.423 MHz as a function of ERP. They defined an absorption index Γ

$$\Gamma = P_T - P_R \tag{5}$$

where P_T and P_R are the pump ERP and received power of the reflected pump expressed in decibels relative to arbitrary, fixed references. Hence Γ can be expressed in terms of several contributions as

$$\Gamma = \Gamma_{\text{anom}} + \Gamma_{\text{D}} + \Gamma_{\text{other}} \tag{6}$$

where Γ_{anom} corresponds to the F-region anomalous absorption due to FAI, Γ_{D} due to D-region absorption and Γ_{other} accounts for experimental and instrumental factors which are assumed constant. Hence, changes in Γ can be interpreted as changes in Γ_{anom} and Γ_{D}.

[33] *Jones et al.* [1983] found that Γ increased by 6–10 dB as the ERP was increased from 32.5 MW to 260 MW. In the present study, the D-region absorption of the pump wave increased by 3.8 dB as the ERP was increased from 38 MW to 202 MW for the 10:00–10:30 UT interval, which had the weakest D-region, hence Γ_{D} increased by 3.8 dB. If similar D-region conditions applied in the experiment analyzed by Jones et al. then about 2–6 dB of the increase in pump absorption was due to the conversion of the pump wave to UH waves and can be assigned to Γ_{anom}. This assumes that the downcoming reflected pump wave did not also pass through the heated D-region (which seems appropriate for the geometry employed in the experiment) and neglects the difference in pump frequency between the case of Jones et al. and that presented here. If the actual (absolute) F-region absorption of the pump was close to zero at an ERP of 32.5 MW then this suggests that as little as 25% of the pump wave was reflected when the ERP was 260 MW. This is roughly consistent with the efficiencies found here for an ERP of 202 MW. The experiment analyzed by *Jones et al.* [1983] used a vertically directed pump wave whereas the present study used a field-aligned pump. It is known that electron heating is higher for field-aligned pumping than for vertical pumping [*Rietveld et al.*, 2003] and so the efficiency may be higher in that case. Measurements of the reflected pump wave during field-aligned pumping would be useful to test this hypothesis.

4.2. Sources of Error

[34] The densities of neutral species used in the calculation of the electron cooling rates and thermal conductivities were taken from the empirical MSISE-90 model [*Hedin*, 1991]. *Mikhailov and Lilensten* [2004] extracted neutral atmosphere parameters from EISCAT measurements using a physical model of the ionosphere and compared the results with those from the MSIS-86 model. They found that while there was reasonably good agreement in quiet geomagnetic conditions, during disturbed conditions MSIS-86 tended to overestimate the neutral densities. The definition of "disturbed" used by *Mikhailov and Lilensten* [2004] is not clear. The daily mean A_p indices for the period 7–14 November 2006 (inclusive) were 0, 0, 10, 36, 21, 7, 1, 5. Thus, the experiment analyzed here was performed on a quiet day three days after some moderate geomagnetic disturbance. On the other hand, *Burke et al.* [2007] compared the thermospheric densities from the NRLMSISE-00 model with those derived from GRACE satellite drag measurements. The comparisons were performed for two large ($D_{st} < -200$ nT) storms and NRLMSISE-00 was found to underestimate the neutral densities during the storms, but was in reasonable agreement during the quiet times. During the disturbed period preceding the experiment described here, D_{st} reached a minimum of only -63 nT on 10 November and varied between -11 and -13 nT during the experiment and it seems unlikely that any storm-related effects on the thermosphere would have been present at that time. Consequently there seems to be no good reason to suspect a large discrepancy from the MSISE-90 model densities used in the analysis, on the basis of geomagnetic activity at least.

[35] The effect of neutral density on the retrieved heating rates was investigated by repeating the model fit to the observations for on-off cycle 6 (10:25–10:30 UT, Figure 2), scaling the neutral densities from the MSISE-90 model. When the densities were scaled by a factor of $\frac{2}{3}$, the height-integrated heating rate was 0.52 times that found for unscaled densities. Scaling the densities by a factor of $\frac{3}{2}$ resulted in a heating rate 1.7 times the value for unscaled densities. This indicates that the estimated heating rates are rather sensitive to the assumed neutral densities and suggests that the effect of neutral density is dominated by its effect on the electron cooling rate, rather than on thermal conductivity.

[36] The pump power flux used to compare with the height-integrated electron heating rate was determined by extrapolating the power flux leaving the D-region to an altitude of 202 km assuming propagation in free space at a zenith angle of 12°. In reality, since the wave frequency is below the critical frequency, it experiences strong refraction and will be reflected back down to the ground. This was investigated by ray-tracing of the pump using a derivative of the *Jones and Stephenson* [1975] code. The electron density profile for the ray-trace was taken to be the median profile over the entire 2-hour interval. The reflection altitude of the field-aligned pump beam was found to be 205 km and as already noted, the UH resonance altitude was 202 km. The divergence of the beam was calculated by tracing a narrow bundle of rays and comparing the cross-sectional area of the bundle to that expected from simple geometry alone at the same range from the transmitter. At the UH resonance altitude, the calculated divergence was found to be 1.27 times that expected from simple geometry, thus the power flux would be 1/1.27 = 0.79 times that calculated geometrically.

[37] *Senior et al.* [2011] compared observations of changes in cosmic noise absorption due to heating of the D-region

with the EISCAT HF facility and found evidence that the ERP of the facility may be overestimated by assuming a perfectly reflecting ground beneath the transmitting antennae. Senior et al. suggested that the ERP could be reduced to 75% of its value for a perfect ground if more realistic ground conductivity was assumed. Combining this factor with that due to beam divergence would scale the power flux S by a factor of 0.59, scaling the efficiency η by a factor of 1.69. This would result in unphysical efficiencies greater than 100% at the higher power fluxes. Possibly this could mitigated if the true neutral density was lower than those given by MSISE-90 or if another factor such as focussing of the pump by a large-scale depletion of electron density in the heated region is important. However, on this latter point, it was noted earlier (Sec. 3.1) that no significant difference in the electron density between heater-on and heater-off was found. It seems that the best that can be said is that the efficiency at high pump power fluxes is very high and probably close to 100%.

[38] In Figure 1 (middle) it can be seen that the height (z_0) of the heat source is quite variable. Excluding the anomalous case of on-off cycle 10, z_0 varies between 196 and 228 km with a median of 209 km, the distribution being skewed toward lower altitudes. As the median of the error estimates for z_0 is 7 km, much of this variability can be explained by measurement uncertainty, but some systematic effects may remain. It is not clear whether this bias is a consequence of systematic error in the model being fitted, or if it represents a genuine indication that the height of maximum heating tends to be higher than the estimated UH resonance height. On the basis of geometry alone, assuming an altitude of 209 km instead of 202 km would reduce the pump power flux by a factor of $(202/209)^2 = 0.93$, increasing the apparent efficiency of the heating.

[39] Finally, it is possible that some of the variability in the height of the electron heat source may be explained by the AGW activity described in Sec. 4.1. Indeed, some degree of correlation between the heights of the heat source and of the UH resonance level is evident in Figure 1.

4.3. D-region Absorption

[40] The observation that the height-integrated heating rates due to pumping are well-ordered by the pump power flux after applying the correction for D-region absorption (Figure 6) suggests that the variability originally shown in Figure 2 is largely explicable by the changes in D-region absorption. The short-term changes in the D-region electron density observed during this experiment (Figure 4) are most likely to be due to energetic electron precipitation, which is common in the auroral zone at the time of day when the experiment was conducted [*Kavanagh et al.*, 2004]. These precipitating electrons, with energies exceeding ~20 keV, produce negligible ionization in the F-region [*Rees*, 1963] and so their presence is not evident from the F-region incoherent scatter measurements alone. Moreover, the absorption may not be sufficient to cause loss of echoes in ionosondes; in the case of this experiment, only a reduction in the E region echoes below about 2 MHz was observed by the Dynasonde. It is evident that when analyzing F-region heating experiments, especially at high latitudes, attention should be paid to the influence of D-region absorption on the F-region heating phenomena.

5. Conclusion

[41] By inverting electron temperature profiles, the electron heat source due to HF radio pumping of the F-region has been extracted. Comparing this to the available pump power flux after correcting for absorption in the D-region reveals that the efficiency of the conversion of pump energy to electron thermal energy increases with pump power and is probably close to 100% at high power fluxes. This seems to be consistent with a theoretical picture of increased conversion of the pump wave to electrostatic UH waves on increasingly intense FAI. Changes in the D-region electron density during the period of the experiment, although small, have a significant effect on the amount of pump power reaching the F-region.

Appendix A: Correction of the Ion Composition Assumed in the UHF Radar Data Analysis

[42] The UHF radar data were analyzed with version 8.6 of the standard GUISDAP analysis software [*Lehtinen and Huuskonen*, 1996]. By default, GUISDAP includes two ion species in the model for the incoherent scatter spectrum, one representing O^+ with a mass of 16 u and one representing a mixture of O_2^+ and NO^+ with a mass of 30.5 u. The ion composition, expressed as the ratio $[O^+]/N_e$ where N_e is the electron density, is determined from the IRI-2007 model [*Bilitza and Reinisch*, 2008] and is held fixed while the other plasma parameters are fitted.

[43] It has previously been found that due to the considerable variability in the ion composition in the high-latitude ionosphere, the ion composition assumed in the analysis may be incorrect [*Shibata et al.*, 2000; *Lathuillère and Kofman*, 2006]. Since the ion mass and temperature both determine the width of the incoherent scatter ion line, an error in the ion composition manifests itself as an error in the fitted ion temperature.

[44] The median ion temperature profile over the 10–12 UT interval using the default ion composition model is shown in Figure A1. The maximum in ion temperature at 185 km is unphysical since the ions are closely coupled to the neutrals and heated mainly by elastic collisions with electrons. To obtain a more realistic profile, the median profile was fitted with a function of the form

$$T_i = \frac{T_{\max} + T_{\min}}{2} + \frac{T_{\max} - T_{\min}}{\pi} \tan^{-1}\left(\frac{z - z_t}{\Delta z}\right) \qquad \text{(A1)}$$

as suggested by *Shibata et al.* [2000], where $T_{\max}$, $T_{\min}$ are maximum and minimum temperatures, z_t is the altitude at which the temperature is halfway between maximum and minimum and Δz is a scale height of the temperature transition. The function was fit to the data below 150 km and between 250 and 450 km altitude and is shown in Figure A1.

[45] The analysis with GUISDAP was then repeated, but this time using this model ion temperature profile and fitting for the ion composition instead of the ion temperature. The

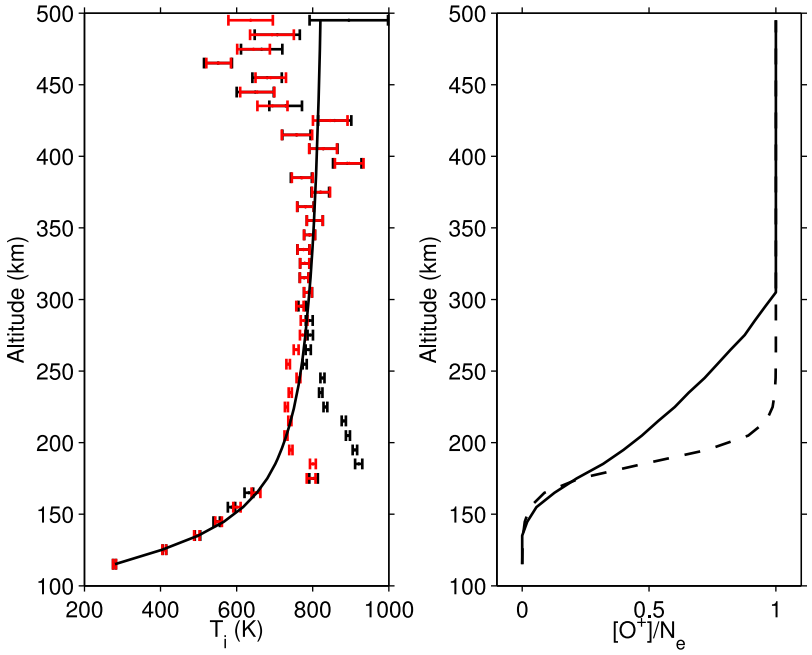

Figure A1. (left) The median ion temperature profile over the 2-hour interval determined using the default ion composition model (black points with error bars), the fit of (A1) to these data (black curve) and the median ion temperature profile using the revised ion composition model (red points with error bars). (right) The default ion composition profile (solid line) and the revised one using the form of (A2).

resulting composition values for the whole 2-hour interval were then fit with a function of the form

$$\frac{[O^+]}{N_e} = \frac{1}{2}\left[1 + \tanh\left(\frac{z - z_t}{\Delta z}\right)\right] \quad \text{(A2)}$$

as suggested by *Lathuillère and Kofman* [2006], where z_t and Δz have similar meanings as in (A1) but in general take different values. The original and fitted composition profiles are shown in the Figure A1 (right). The result shows that the anomalous peak in ion temperature is a result of the proportion of molecular ions being overestimated in the default composition model.

[46] Finally, as a check, the data were re-analyzed again with GUISDAP using this new ion composition profile and fitting for the ion temperature in the normal way. The fitted ion temperatures resulting from this are shown in red in Figure A1 (left). Although the anomalous maximum has not been completely eliminated, it is greatly reduced compared to the original analysis. The reason for the apparent minimum in ion temperature around an altitude of 450 km in both the original and final analyses is not understood, but is unlikely to be a real feature.

[47] In the analysis of Section 3, the ion temperature profile assumed in the electron temperature model was taken directly from the fitted profile (A1) and the ion composition profile directly from (A2). The electron temperatures were determined from the electron-ion temperature ratios found in the corrected analysis and the model ion temperature profile (A1).

[48] **Acknowledgments.** Solar and geomagnetic indicies were obtained from the UK Solar System Data Centre and the WDC for Geomagnetism, Kyoto. EISCAT is an international association supported by research organizations in China (CRIRP), Finland (SA), Germany (DFG), Japan (NIPR and STEL), Norway (NFR), Sweden (VR), and the United Kingdom (NERC). This work was supported by STFC grant ST/G00241X/1. The work by T.K.Y. is supported by STFC grant ST/H002480/1. The Hankasalmi SuperDARN radar operations were funded by STFC grant PP/E007929/1.

[49] Robert Lysak thanks the reviewers for their assistance in evaluating this paper.

References

Bilitza, D., and B. W. Reinisch (2008), International Reference Ionosphere 2007: Improvements and new parameters, *Adv. Space Res.*, *42*, 599–609, doi:10.1016/j.asr.2007.07.048.

Booker, H. G. (1956), A theory of scattering by nonisotropic irregularities with application to radar reflections from the aurora, *J. Atmos. Terr. Phys.*, *8*, 204–221.

Burke, W. J., C. Y. Huang, F. A. Marcos, and J. O. Wise (2007), Interplanetary control of thermospheric densities during large magnetic storms, *J. Atmos. Sol. Terr. Phys.*, *69*, 279–287.

Campbell, L., M. J. Brunger, D. C. Cartwright, and P. J. O. Teubner (2004), Production of vibrationally excited N_2 by electron impact, *Planet. Space Sci.*, *52*, 815–822.

Chisham, G., et al. (2007), A decade of the Super Dual Auroral Radar Network (SuperDARN): Scientific achievements, new techniques and future directions, *Surv. Geophys.*, *28*, 33–109, doi:10.1007/s10712-007-9017-8.

Dysthe, K. B., E. Mjølhus, H. L. Pécseli, and K. Rypdal (1983), A thermal oscillating two-stream instability, *Phys. Fluids*, *26*(1), 146–157.

Greenwald, R. A., et al. (1995), DARN/SUPERDARN: A global view of the dynamics of high-latitude convection, *Space Sci. Rev.*, *71*, 761–796.

Gustavsson, B., T. B. Leyser, M. Kosch, M. T. Rietveld, Å. Steen, B. U. E. Brändström, and T. Aso (2006), High-latitude pump-induced optical emissions for frequencies close to the third electron gyro-harmonic, *Phys. Rev. Lett.*, *97*, 195002, doi:10.1103/PhysRevLett.97.195002.

Gustavsson, B., M. T. Rietveld, N. V. Ivchenko, and M. J. Kosch (2010), Rise and fall of electron temperatures: Ohmic heating of ionospheric electrons from underdense HF radio wave pumping, *J. Geophys. Res.*, *115*, A12332, doi:10.1029/2010JA015873.

Hedberg, Å., H. Derblom, G. Hamberg, B. Thidé, H. Kopka, and P. Stubbe (1986), Measurements of HF backscatter cross section for striations created by ionospheric heating at different power levels, *Radio Sci.*, *21*, 117–125.

Hedin, A. E. (1991), Extension of the MSIS thermosphere model into the middle and lower atmosphere, *J. Geophys. Res.*, *96*, 1159–1172.

Honary, F., T. R. Robinson, D. M. Wright, A. J. Stocker, M. T. Rietveld, and I. McCrea (1999), First direct observations of the reduced striations at pump frequencies close to the electron gyroharmonics, *Ann. Geophys.*, *17*, 1235–1238.

Jones, D. B., L. Campbell, M. J. Bottema, and M. J. Brunger (2003), New electron-energy transfer rates for vibrational excitation of O_2, *New J. Phys.*, *5*, 114–125.

Jones, R. M., and J. J. Stephenson (1975), A versatile three-dimensional ray tracing computer program for radio waves in the ionosphere, *Tech. Rep. OT 75-76*, Office of Telecommun., U. S. Dept. of Commerce, Washington, D. C.

Jones, T. B., T. R. Robinson, P. Stubbe, and H. Kopka (1983), A hysteresis effect in the generation of field-aligned irregularities by a high-power radio wave, *Radio Sci.*, *18*, 835–839.

Jones, T. B., T. R. Robinson, P. Stubbe, and H. Kopka (1986), EISCAT observations of the heated ionosphere, *J. Atmos. Terr. Phys.*, *48*, 1027–1035.

Kavanagh, A. J., M. J. Kosch, F. Honary, A. Senior, S. R. Marple, E. E. Woodfield, and I. W. McCrea (2004), The statistical dependence of auroral absorption on geomagnetic and solar wind parameters, *Ann. Geophys.*, *22*, 877–887.

Kosch, M. J., M. T. Rietveld, A. J. Kavanagh, C. Davis, T. K. Yeoman, F. Honary, and T. Hagfors (2002), High-latitude pump-induced optical emissions for frequencies close to the third electron gyro-harmonic, *Geophys. Res. Lett.*, *29*(23), 2112, doi:10.1029/2002GL015744.

Kosch, M. J., et al. (2009), First incoherent scatter radar observations of ionospheric heating on the second electron gyro-harmonic, *J. Atmos. Sol. Terr. Phys.*, *71*, 1959–1966, doi:10.1016/j.jastp.2009.08.007.

Lathuillère, C., and W. Kofman (2006), A short review on the F1-region ion composition in the auroral and polar ionosphere, *Adv. Space Res.*, *37*, 913–918.

Lehtinen, M. S., and A. Huuskonen (1996), General incoherent scatter analysis and GUISDAP, *J. Atmos. Terr. Phys.*, *58*, 435–452.

Lester, M., et al. (2004), Stereo CUTLASS—A new capability for the SuperDARN HF radars, *Ann. Geophys.*, *22*, 459–473.

Mantas, G. P., H. C. Carlson, and C. H. LaHoz (1981), Thermal response of the F region ionosphere in artificial modification experiments by HF radio waves, *J. Geophys. Res.*, *86*, 561–574.

Mikhailov, A. V., and J. Lilensten (2004), A revised method to extract thermospheric parameters from incoherent scatter observations, *Ann. Geophys.*, *47*(2–3), 985–1008.

Pavlov, A. V. (1998a), New electron energy transfer rates for vibrational excitation of N_2, *Ann. Geophys.*, *16*, 176–182.

Pavlov, A. V. (1998b), New electron energy transfer and cooling rates by excitation of O_2, *Ann. Geophys.*, *16*, 1007–1013.

Pavlov, A. V., and K. A. Berrington (1999), Cooling rate of thermal electrons by electron impact excitation of fine structure levels of atomic oxygen, *Ann. Geophys.*, *17*, 919–924.

Rees, M. H. (1963), Auroral ionization and excitation by incident energetic electrons, *Planet. Space Sci.*, *11*, 1209–1218.

Rietveld, M. T., H. Kohl, H. Kopka, and P. Stubbe (1993), Introduction to ionospheric heating experiments at Tromsø-I. Experimental overview, *J. Atmos. Terr. Phys.*, *55*, 577–599.

Rietveld, M. T., M. J. Kosch, N. F. Blagoveshchenskaya, V. A. Kornienko, T. B. Leyser, and T. K. Yeoman (2003), Ionospheric electron heating, optical emissions, and striations induced by powerful HF radio waves at high latitudes: Aspect angle dependence, *J. Geophys. Res.*, *108*(A4), 1141, doi:10.1029/2002JA009543.

Rietveld, M. T., J. W. Wright, N. Zabotin, and M. L. V. Pitteway (2008), The Tromsø dynasonde, *Polar Sci.*, *2*, 55–71, doi:10.1016/j.polar.2008.02.001.

Rishbeth, H., and A. P. van Eyken (1993), EISCAT–Early history and the first ten years of operation, *J. Atmos. Terr. Phys.*, *55*(4–5), 525–542.

Robinson, T. R. (1989), The heating of the high latitude ionosphere by high power radio waves, *Phys. Rep.*, *179*, 79–209.

Robinson, T. R., F. Honary, A. J. Stocker, T. B. Jones, and P. Stubbe (1996), First EISCAT observations of F-region electron temperature during RF heating at harmonics of the electron gyrofrequency, *J. Atmos. Terr. Phys.*, *58*, 385–395.

Schunk, R. W., and A. F. Nagy (1978), Electron temperatures in the F region of the ionosphere: Theory and observations, *Rev. Geophys.*, *16*(3), 355–399.

Schunk, R. W., and A. F. Nagy (2000), *Ionospheres: Physics, Plasma Physics, and Chemistry*, Cambridge Univ. Press, New York.

Senior, A., M. J. Kosch, T. K. Yeoman, M. T. Rietveld, and I. W. McCrea (2006), Effects of high-latitude atmospheric gravity wave disturbances on artificial HF radar backscatter, *Ann. Geophys.*, *24*, 2347–2361.

Senior, A., M. T. Rietveld, M. J. Kosch, and W. Singer (2010), Diagnosing radio plasma heating in the polar summer mesosphere using cross-modulation: Theory and observations, *J. Geophys. Res.*, *115*, A09318, doi:10.1029/2010JA015379.

Senior, A., M. T. Rietveld, F. Honary, W. Singer, and M. J. Kosch (2011), Measurements and modelling of cosmic noise absorption changes due to radio heating of the D region ionosphere, *J. Geophys. Res.*, *116*, A04310, doi:10.1029/2010JA016189.

Shibata, T., H. Matsuya, and J. Hoashi (2000), Ion composition in the auroral lower F-region inferred from residuals of ion temperature profiles observed with EISCAT, *Adv. Space Res.*, *25*(1), 201–210.

Stocker, A. J., F. Honary, T. R. Robinson, T. B. Jones, P. Stubbe, and H. Kopka (1992), EISCAT observations of large scale electron temperature and electron density perturbations caused by high power HF radio waves, *J. Atmos. Terr. Phys.*, *54*, 1555–1572.

Thome, G. D., and D. W. Blood (1974), First observations of RF backscatter from field-aligned irregularities produced by ionospheric heating, *Radio Sci.*, *9*(11), 917–921.

Wright, D. M., J. A. Davies, T. K. Yeoman, T. R. Robinson, and H. Shergill (2006), Saturation and hysteresis effects in ionospheric modification experiments observed by the CUTLASS and EISCAT radars, *Ann. Geophys.*, *24*, 543–553.

M. J. Kosch and A. Senior, Department of Physics, University of Lancaster, Lancaster LA1 4YB, UK. (a.senior@lancaster.ac.uk)

M. T. Rietveld, EISCAT Scientific Association, Ramfjordmoen, N-9027 Ramfjordbotn, Norway.

T. K. Yeoman, Department of Physics and Astronomy, University of Leicester, University Road, Leicester LE1 7RH, UK.